of the leading-edge boundary layer resulting in an apparent increase of the "effective Reynolds number."

References

[1] Carta, F. O., "Unsteady Normal Forces on an Airfoil in a Periodically Stalled Inlet Flow," *Journal of Aircraft*, Vol. 4, No. 5, Sept.-Oct. 1967, pp. 416–421.

[2] Liiva, J., "Unsteady Aerodynamic and Stall Effects on Helicopter Rotor Blade Airfoil Sections," *Journal of Aircraft*, Vol. 6, No. 1, Jan.-Feb. 1969, pp. 46–51.

[3] Halfman, R. L., Johnson, H. C., and Haley, S. M., "Evaluation of High-Angle-of-Attack Aerodynamic-Derivative Data and Stall-Flutter Prediction Techniques," TN 2533, 1951, NACA.

[4] Rainey, A. G., "Measurement of Aerodynamic Forces for Various Mean Angles of Attack of an Airfoil Oscillating in Pitch and on Two Finite-Span Wings Oscillating in Bending with Emphasis on Damping in the Stall," TN 3643, 1955, NACA.

[5] Harris, F. D., and Pruyn, R. P., "Blade Stall—Half Fact, Half Fiction," *American Helicopter Society Journal*, Vol. 13, No. 4, April 1968, pp. 27–48.

[6] Ericsson, L. E., and Reding, J. P., "Analysis of Flow Separation Effects of the Dynamics of a Large Space Booster," *Journal of Spacecraft and Rockets*, Vol. 2, No. 4, July-Aug. 1965, pp. 481–490.

[7] Ericsson, L. E. and Reding, J. P., "Dynamic Stability Problems Associated with Flare Stabilizers and Flap Controls," AIAA Paper 69-182, New York, Jan. 1969.

[8] von Kármán, T. and Sears, W. R., "Airfoil Theory for Non-Uniform Motion," *Journal of the Aerospace Sciences*, Vol. 5, No. 10, Aug. 1938, pp. 379–390.

[9] Multhopp, H., "Die Berechnung der Auftriebsverteilung von Trafluegeln," *Luftfahrt Forschung*, Bd. 15, 1938, p. 153.

[10] Lomax, H., Heaslet, M. A., Fuller, F. B., and Sluder, L., "Two and Three-Dimensional Unsteady Lift Problems in High-Speed Flight," Rept. 1077, 1952, T.R., p. 18.

[11] Conner, F., Willey, C., and Twomey, W., "A Flight and Wind Tunnel Investigation of the Effect of Angle-of-Attack Rate on Maximum Lift Coefficient," CR-321, 1965, NASA.

[12] Harper, P. W., and Flanigan, R. E., The Effect of Rate of Change of Angle of Attack on the Maximum Lift of a Small Model," TN 2061, 1949, NACA.

[13] Ericsson, L. E., "Comment on Unsteady Airfoil Stall," *Journal of Aircraft*, Vol. 4, No. 5, Sept.-Oct. 1967, pp. 478–480.

[14] Ericsson, L. E., "Loads Induced by Terminal-Shock Boundary-Layer Interaction on Cone-Cylinder Bodies," *Journal of Spacecraft and Rockets*, Vol. 7, No. 9, Sept. 1970, pp. 1106–1112.

[15] Ericsson, L. E., Aeroelastic Instability Caused by Slender Payloads," *Journal of Spacecraft and Rockets*, Vol. 4, No. 1, Jan. 1967, pp. 65–73.

[16] Ericsson, L. E., and Reding, J. P., "Unsteady Airfoil Stall," CR 66787, 1969, NASA.

[17] Kline, S. J., "Some New Concepts of the Mechanics of Stall in Turbulent Boundary Layers," *Journal of the Aerospace Sciences*, Vol. 24, No. 6, June 1957, pp. 470–471.

[18] Sarpkaya, T., "Separated Unsteady Flow About a Rotating Plate," *Proceedings of the Tenth Midwestern Mechanics Conference: Developments in Mechanics*, Vol. 4, 1968, pp. 1485–1499.

[19] Ham, N. D., "Aerodynamic Loading on a Two-Dimensional Airfoil during Dynamic Stall," *AIAA Journal*, Vol. 6, No. 10, Oct. 1968, pp. 1927–1934.

AUGUST 1971 J. AIRCRAFT VOL. 8, NO. 8

T-Tail Transport Empennage Loads in Continuous Atmospheric Turbulence

H. M. DODD JR.*
Sandia Laboratories, Albuquerque, N. Mex.

AND

K. G. PRATT†
NASA Langley Research Center, Hampton, Va.

Empennage loads on a T-tail transport were determined for simultaneous application of vertical and lateral gust components of atmospheric turbulence. A real-time analog-digital computer simulation employing data from tests in the NASA Langley transonic dynamics tunnel investigated the relative importance of nonlinear effects caused by the combined gusts. These effects were found to be negligible, but the linear contributions of the lateral gust on the horizontal stabilizer load were found to be significant. Results are presented in the form of power spectral densities and load exceedance rates that indicate how much the expected maximum stabilizer load is increased when combined gusts are considered.

Nomenclature

A = tail total angle of attack due to motion and gust for zero mean load
$\bar{A}$ = ratio of rms output response to rms gust input
a_y,a_z = lateral and vertical acceleration of a point on the empennage
B,BH = vertical tail and horizontal stabilizer total angles of sideslip due to motion and gust
$BM1,2,3$ = bending moments in horizontal stabilizer, fin tip, and fin root
b = span of wing
C_{ij} = nondimensional empennage load coefficient [see Eq. (10)]
$\bar{c}$ = wing mean aerodynamic chord
$d(\eta)$ = perpendicular distance from elemental mass location to bending moment axis
f_0 = natural frequency, Hz
f_{v_g},f_{w_g} = lateral and vertical gust forces
H = complex one-dimensional frequency response function

Presented at the AIAA/ASME 11th Structures, Structural Dynamics, and Materials Conference, Denver, Colo., April 22–24, 1970 (no paper number; published in bound volume of conference papers); submitted June 5, 1970; revision received February 17, 1971. This work was conducted under NASA Research Grant NGR-17-002-047 to the University of Kansas.

[*] Member of the Technical Staff, Systems Environmental Testing Department.

[†] Aerospace Technologist, Aerodynamic Loads Branch, Loads Division. Member AIAA.

i = incidence angle
k_1,k_2 = longitudinal $(\omega\bar{c}/2u_0)$ and lateral $(\omega b/2u_0)$ reduced frequencies
k' = reduced frequency, $\omega L/u_0$
l = length between wing and tail
L = atmospheric scale of turbulence
$m(\eta)$ = distributed tail masses
N_0 = average number of zero load crossings with positive slope per unit time
$N(x)$ = average number of load crossings of level x with positive slope per unit time
s_1,s_2 = complex longitudinal and lateral reduced frequencies, ik_1 and ik_2
u_0 = airplane freestream velocity
v_g,w_g = lateral and vertical gust velocities
α = stability axis angle of attack, w/u_0, rad
α_{WT} = wind-tunnel body axis angle of attack
β = stability axis angle of sideslip, v/u_0
ϵ_0 = tail downwash angle at level flight conditions
ζ = damping ratio
η_H,η_T = nondimensional stabilizer semispan coordinate $(2y/B_H)$ and fin coordinate $(-z/b_T)$
θ = pitch angle, rad
σ = root-mean-square value
τ_1,τ_2 = time lag between c.g. and stabilizer (l_H/u_0) and fin (l_T/u_0) for gust penetration effect
ϕ = roll angle, rad
Φ = power spectrum
ψ = yaw angle, rad
ω = circular frequency, rad/sec

Subscripts

D,F,V = Dryden, analog filter, and von Kármán gust representations
FW = fuselage wing
G,g = gust
H = horizontal stabilizer
I = inertia
M = motion
T = vertical tail
W = wing
1 = airplane longitudinal equations
2 = airplane lateral equations

Introduction

IN the fall of 1966, a commercial T-tail transport crashed while approaching a thunderstorm, and evidence from the wreckage indicated that a gust overload caused the horizontal stabilizer and vertical fin to fail.[1] This accident raised questions concerning design methods and requirements for handling the gust loads on T-tailed aircraft. Builders of T-tail transport airplanes have conducted extensive analyses of the gust loads on the tail surfaces for their own particular configurations. However, practically none of the results are available in the open literature. The Langley Research Center, therefore, considered desirable an exploration of some aspects of this general problem. The highlights of the study and some of the results are described herein.

Airworthiness standards for transport airplanes[2] specify empennage gust load design procedures in which the empennage is loaded in response to the vertical component of atmospheric turbulence and to the lateral component as separate design conditions, that is, simultaneous response to vertical and lateral components is not required. These separate design conditions together with the possibility of unusual aerodynamic interference effects on the T-tail configuration prompted a study of interactions involving additional loads on the horizontal surface from responses to the lateral component of turbulence and loads on the vertical surface from responses to the vertical component; both components of turbulence acting simultaneously and continuously as they do in the atmosphere.

Tail loads were determined in terms of bending moments on the stabilizer and fin of a rigid but otherwise representative T-tailed transport in a cruise flight condition. The short-period longitudinal mode and the lateral modes of motion were simulated on an analog computer. The equations for tail loads provided for quasi-steady aerodynamic interference effects that were determined from wind-tunnel tests for combined angles of attack and sideslip. The turbulence velocity components were simulated by two separate, appropriately filtered noise generators. The random loads were statistically analyzed by a digital computer and results were obtained in the form of power spectral density functions and load exceedance rates. The results were examined for effects of nonlinear relations between loads and turbulence intensity and were compared to results based on loads from each turbulence component acting separately, as specified in the Airworthiness Standards.

Airplane Representation

Mathematical Model

Since this study is exploratory in nature, the airplane was approximated by the simplest model that was felt to retain the essential loading characteristics of the T-tail configuration. Specifically, the geometry selected is representative of a large jet transport or cargo airplane. The structure is considered a rigid body and the airplane motion is described by degrees of freedom in plunge, pitch, sideslip, roll, and yaw.

Equations of Motion

The motions and the resulting forces are related by the classical equations for dynamic stability plus certain additional terms that describe nonlinear force and motion relations. The coordinate system used to describe the motion is shown in Fig. 1, and the resulting equations, using the notation of Etkin,[3] are expressed in matrix form

$$\begin{Bmatrix}\alpha\\ \theta\end{Bmatrix} = [M]^{-1}\{f_{w_g}\} \tag{1}$$

$$\begin{Bmatrix}\beta\\ \phi\\ \psi\end{Bmatrix} = [N]^{-1}\{f_{v_g}\} \tag{2}$$

where

$$[M] = \begin{bmatrix}(2\mu_1 - C_{z_{\dot{\alpha}}})D_1 - C_{z\alpha} & -(2\mu_1 + C_{z_q})D_1\\ -(C_{m_{\dot{\alpha}}}D_1 + C_{m\alpha}) & (i_BD_1 - C_{m_q})D_1\end{bmatrix} \tag{3}$$

$$[N] = \begin{bmatrix}(2\mu_2D_2 - C_{Y\beta}) & -(C_{Y_p}D_2 + C_{L_0}) & (2\mu_2 - C_{Y_r})D_2\\ -C_{l\beta}(\alpha) & (i_AD_2 - C_{l_p})D_2 & -[i_ED_2 + C_{l_r}(\alpha)]D_2\\ -C_{n\beta}(\alpha) & -[i_ED_2 + C_{n_p}(\alpha)]D_2 & (i_CD_2 - C_{n_r})D_2\end{bmatrix} \tag{4}$$

where D_1 and D_2 are nondimensional time derivatives ($D_1 = c/2u_0\cdot d/dt$, $D_2 = b/2u_0\cdot d/dt$) and $\{f_{w_g}\}$ and $\{f_{v_g}\}$ are the generalized vertical and lateral gust forces of atmospheric turbulence.

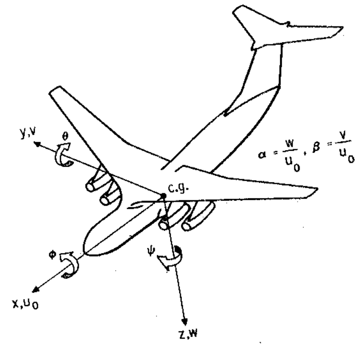

Fig. 1 Airplane stability axis coordinates.

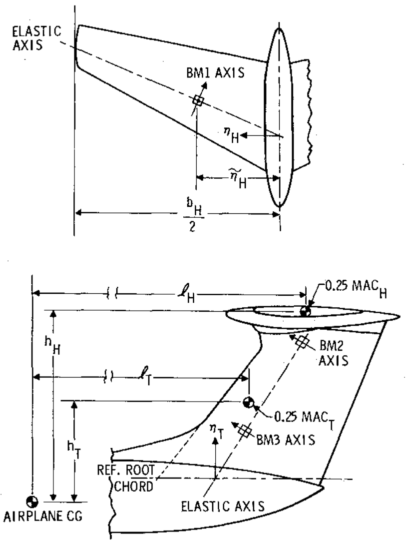

Fig. 2 Empennage coordinates.

Aerodynamic Forces

Forces due to airplane motion are treated as quasi-static forces using the conventional stability equations expressed in terms of stability derivatives except for the following terms: the lateral derivatives $C_{l\beta}$, C_{l_r}, $C_{n\beta}$, and C_{n_p} are considered functions of airplane angle of attack (see Chaps. 3 and 5 of Ref. 3), and hence the motion equations are nonlinear. The effects of a yaw damper are approximated by an appropriate decrease in the value of C_{n_r}.

The gust forces, f_{w_g} and f_{v_g}, are also treated as quasi-steady and are expressed in terms of the gust forces on wing and tail surfaces individually. Gust penetration is accounted for by transport lags $\tau_1 = l_H/u_0$ and $\tau_2 = l_T/u_0$. The gust forces are expressed as

$$\{f_{w_g}\} = -\frac{1}{u_0}\begin{bmatrix}(C_{z\alpha})_W & (C_{z\alpha})_H \\ (C_{m\alpha})_W & (C_{m\alpha})_H\end{bmatrix}\begin{Bmatrix}w_g(t) \\ w_g(t-\tau_1)\end{Bmatrix} \tag{5}$$

$$\{f_{v_g}\} = -\frac{1}{u_0}\begin{bmatrix}(C_{Y\beta})_{FW} & (C_{Y\beta})_T \\ (C_{l\beta})_{FW} & (C_{l\beta})_T \\ (C_{n\beta})_{FW} & (C_{n\beta})_T\end{bmatrix}\begin{Bmatrix}v_g(t) \\ v_g(t-\tau_2)\end{Bmatrix} \tag{6}$$

Tail Loads

Tail loads are obtained by a summation of aerodynamic loads from airplane motion and gust velocities and inertia loads from accelerations. For this investigation representative tail loads are expressed as bending moments at selected locations on the stabilizer and fin. Figure 2 shows the locations chosen (denoted BM1, BM2, and BM3) and also defines the tail geometry necessary for the load computations.

For the case of tail aerodynamic loads, the combination of body motions and gust velocities can be defined by total angle of attack and sideslip in the form

$$A(t) = \alpha(t) - (d\epsilon/d\alpha)\alpha(t-\tau_1) + (1/u_0)[l_H\dot{\theta} - (1 - \{d\epsilon/d\alpha\})w_g(t-\tau_1)] \tag{7}$$

$$B(t) = \beta(t) + (1/u_0)[h_T\dot{\varphi} - l_T\dot{\psi} - v_g(t-\tau_2)] \tag{8}$$

$$BH(t) \doteq B(t) + (1/u_0)[(h_H - h_T)\dot{\varphi} - (l_H - l_T)\dot{\psi}] \tag{9}$$

where A is the stabilizer angle of attack, B is the fin angle of sideslip, and BH is an approximation to the stabilizer angle of sideslip for a T-tail. The constant downwash term ϵ_0 and tail incidence angle i_H are neglected in A because ϵ_0 and i_H represent only a constant download for undisturbed flight which will be included later.

The bending moment at station i due to the aerodynamic loads is approximated by a polynomial of the form

$$(BMi)_{M+G} = C_{i1}A + C_{i2}B + C_{i3}A^2 + C_{i4}AB + C_{i5}B^2 \tag{10}$$

where the coefficients C_{ij} are constants to be discussed later and A and B are defined by Eqs. (7) and (8) or (9).

The inertia loads are formulated from the accelerations, the geometry, and the mass distributions. For example, the stabilizer bending moment due to inertia is

$$(BM1)_I = \int_{\tilde{\eta}_H}^{1} m(\eta_H)a_z(\eta_H)d(\eta_H)d\eta \tag{11}$$

where η_H is the nondimensional stabilizer spanwise coordinate, $\tilde{\eta}_H$ is the intersection of the elastic axis and bending-moment axis, m is the mass distribution, and d is the perpendicular distance from the elemental mass at η_H to the bending-moment axis. The vertical and lateral accelerations, a_z and a_y, at a point on the tail are given by

$$a_z = -[(b_H/2)\eta_H\ddot{\varphi} + (l_H' + (b_H/2)\eta_H \sin\Lambda_H)\ddot{\theta} + u_0(\dot{\alpha} - \dot{\theta})] \tag{12}$$

$$a_y = [h'\ddot{\varphi} - l'\ddot{\psi} + u(\dot{\beta} + \dot{\psi})] \tag{13}$$

where b_H is the stabilizer span, l_H' is the horizontal distance from the airplane c.g. to the intersection of the tail elastic axis and airplane vertical plane of symmetry, and Λ_H is the sweep angle of the elastic axis, and where h' and l' are vertical and horizontal distances which may be functions of η_H or η_T. For example, for the stabilizer

$$l' = l_H' + (b_H/2)\ (\sin\Lambda_H)\eta_H$$

The fin inertia bending moment is expressed in a form similar to Eq. (11); however, for a T-tail the stabilizer and bullet nacelle inertia effects must also be included.

The total bending moments at the various empennage locations are then

$$BMi = (BMi)_{M+G} - (BMi)_I \tag{14}$$

Turbulence Representation

Atmospheric turbulence experienced by airplanes is, of course, a random variation of air velocities that is intermittent, and variable in intensity. Current practice is to consider this turbulence experience as synthesized from many short patches of turbulence of various intensities, each of which is assumed to be isotropic, statistically stationary and having a Gaussian probability density. This patch concept is the representation of turbulence for the present study.

The statistical properties include: 1) no correlation between the vertical and lateral velocity components, and 2) equality of mean-square values of the components, that is, $\bar{w}_g^2 = \bar{v}_g^2$. The statistical nature of the turbulence is further described by a power spectrum. Both of the two commonly used mathematical formulations of the transverse velocity components,[4] the Dryden and the von Kármán, are employed in this study.

The Dryden spectrum is defined by

$$[\Phi_g(\omega)]_D = (\bar{w}_g^2L/\pi u_0)[1 + 3(k')^2]/[1 + (k')^2]^2 \tag{15}$$

and the von Kármán by

$$[\Phi_g(\omega)]_V = (\bar{w}_g^2L/\pi u_0)\cdot[1 + \tfrac{8}{3}(1.339k')^2]/[1 + (1.339k')^2]^{11/6} \tag{16}$$

where

$$k' = L\omega/u_0$$

The von Kármán spectrum is considered the more realistic model of the atmosphere. However, the Dryden spectrum is mathematically somewhat simpler and is often used in exploratory studies.

It should be noted that the turbulence model is one-dimensional; that is, the gust velocities are assumed to vary in the direction of flight and to be invariant along the span as is implied by the form of the gust forces in Eqs. (5) and (6).

Solutions for Tail Loads

Nonlinear Equations

Solutions of Eqs. (1–12) were obtained by an analog simulation for a representative airplane configuration using vertical and lateral turbulence velocities having an approximate Dryden power spectrum. The simulation is broadly indicated by the block diagram on the left side of Fig. 3. Each turbulence velocity component was separately simulated by an electronic white noise generator passed through a first-order band-pass filter as diagramed in Fig. 4.

The bending-moment response and gust input random time functions were analyzed statistically with a digital computer to determine mean values, mean-square values, probability distributions, chi-squared test for Gaussian distribution, average frequency of load level crossings, autocorrelation functions, and power spectral density functions as indicated on the right side of Fig. 3.

Solutions of Eqs. (1–6), linearized by removing the dependency of $C_{l\beta}$, C_{l_r}, $C_{n\beta}$, and C_{n_p} on α, were also obtained from the analog simulation. In this case the airplane motion equations are uncoupled into the familiar longitudinal and lateral independent sets of equations.

Linear Equations

Solutions of the linear airplane equations and the loads equations with the coefficients C_{i3}–C_{i5} in Eq. (10) set to zero were obtained both from the analog simulator and by analytical means. The simulator results were compared with the analytical results in order to assess the accuracy of the simulator system.

The analytical solutions were obtained in terms of frequency response functions to a sinusoidal gust field using the uncoupled longitudinal and lateral motion equation sets individually. For this purpose the gust velocities in Eqs. (5) and (6) were replaced by complex exponentials so that

$$w_g(t - \tau_1) \rightarrow w_g \exp(-il_H k'/L) \tag{17a}$$

$$v_g(t - \tau_2) \rightarrow v_g \exp(-il_T k'/L) \tag{17b}$$

Equations (1–4) are Fourier transformed, so they become complex frequency response functions $H_\alpha(k')$, $H_\theta(k')$, and so forth. Substitution of these responses into Eqs. (7–9) provide solutions for tail angles of attack and sideslip. Similar substitutions into Eqs. (11–13) yield inertia frequency responses, and combining these results gives a bending-moment frequency response function analogous to Eq. (14).

The statistical quantites of interest are then obtained from these frequency response functions, $H_R(k')$, and the power spectra of the vertical and lateral gust components. Since $\Phi_{w_g} = \Phi_{v_g} = \Phi_g$, the following relations can be written from random process theory[4,5]:

Response spectrum,

$$\Phi_R = (|H_{R,w_g}|^2 + |H_{R,v_g}|^2)\Phi_g \tag{18}$$

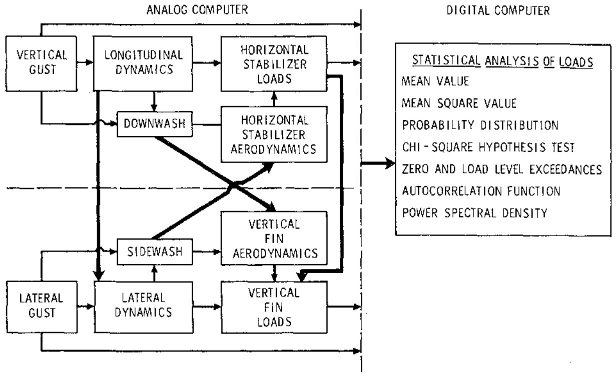

Fig. 3 Computer simulation techniques.

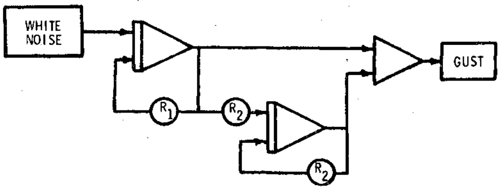

Fig. 4 Analog model for continuous turbulence.

where subscript R denotes any given response.

Mean-square response,

$$\sigma_R^2 = \int_0^\infty \Phi_R dk' \tag{19}$$

Sensitivity factor,

$$\bar{A}_R = \sigma_R/\sigma_g \tag{20}$$

where

$$\sigma_g^2 = \int_0^\infty \Phi_g dk' \tag{21}$$

Average frequency of zero crossing with positive slope,

$$N_{0R} = (u_0/2\pi L)\left[\int_0^\infty k'^2 \Phi_R dk' \Big/ \sigma_R^2\right]^{1/2} \tag{22}$$

Average frequency of crossing level x with positive slope,

$$N(x)_R = N_{0R} \exp(-x^2/2\sigma_R^2) \tag{23}$$

Wind-Tunnel Tests

The lack of information in the literature on both experimental and theoretical T-tail loads under combined angles of attack and sideslip led to the choice of special wind-tunnel tests to provide the necessary data. (Calculation of the theoretical loads by nonplanar lifting-surface methods was considered impracticable because no program was at hand that had been proven by comparison of calculated and experimental results.) In tests conducted in the 16-ft transonic dynamics tunnel at the Langley Research Center, the bending moments BM1, BM2, and BM3 on the stabilizer and fin, previously referred to with respect to Fig. 2 and Eq. (10), were obtained from strain measurements on an essentially rigid model. In addition to empennage loads, total airplane forces and the relative contributions of wing and tail components to these forces were obtained using the equipment indicated in Fig. 5. To measure total forces, the model was supported by a single balance (number 1 in Fig. 5) with a separation plate holding the fore and aft model parts together; then to measure separate wing and tail terms a second balance (number 2) was installed and the separation plate removed. This was necessary in order to define the lagged forces in Eqs. (5) and (6).

The data obtained define a load "surface;" that is, the load (bending moment or airplane force) is expressed as a function of the tunnel body axes' two independent variables, α_{WT} and β. A second-order polynomial is determined from the nondimensionalized data by means of a least-squares fit; and the independent variable α_{WT} is transformed to stability axis angle of attack for a specified flight condition so that each load is finally expressed in the form

$$\text{Load} = C_1 + C_2\alpha + C_3\beta + C_4\alpha^2 + C_5\alpha\beta + C_6\beta^2 \tag{24}$$

where α and β are referenced to stability axes. For example, if the load is total lift C_1 is C_{L_0} and C_2 is $C_{L\alpha}$ and the other C_i's should be zero. However, if the load is one of the empennage bending moments some of the out-of-plane coefficients may be nonzero (e.g., C_3 for stabilizer bending moment). Second-order or nonlinear effects are present if any of the $C_4 - C_6$ coefficients are significant.

For the case of empennage bending moments, the independent variables α and β given in Eq. (24) must be trans-

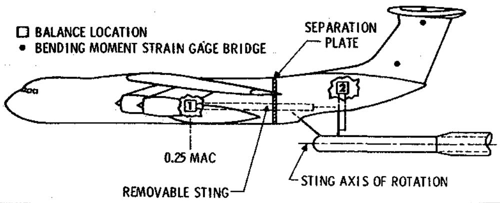

Fig. 5 Force-measuring techniques for wind-tunnel model.

formed to tail angles of attack and sideslip before the results can be applied to the dynamic motions defined by Eqs. (1–4). The total tail angle of attack α_T is

$$\alpha_T = (1 - \partial\epsilon/\partial\alpha)\alpha - (\epsilon_0 + i_H) \tag{25}$$

where i_H is the tailplane geometric angle of attack relative to the stability x-axis, and ϵ_0 and $\partial\epsilon/\partial\alpha$ are wing downwash effects. The values of ϵ_0 and $\partial\epsilon/\partial\alpha$ were determined from a third model configuration in which the wing and forward fuselage were replaced by a simple forebody. The changes in

$$(C_{L\alpha})_{\text{tail}} \text{ and } (C_{L0})_{\text{tail}}$$

between this configuration and the previous one yielded the values of ϵ_0 and $\partial\epsilon/\partial\alpha$. For the horizontal stabilizer, the constant load created by ϵ_0 and i_H was removed for the computer simulation and is added back when considering the total loads.

The tail angle of attack, neglecting the constant downwash, is given by

$$A = \alpha(1 - \partial\epsilon/\partial\alpha) \tag{26}$$

Once the assumption of quasi-steady aerodynamics is applied, A becomes identical to the A defined in Eq. (7), and the steady-state load coefficients determined by putting Eq. (26) into Eq. (24) become the coefficients of the dynamic loads defined by Eq. (10).

Results and Discussion

The general configuration of the example airplane is illustrated in Fig. 1. Some pertinent physical dimensions are listed in Table 1, and the flight parameters for the simulation and analytical solutions are indicated in Table 2.

Verification of Turbulence Simulation

Time functions of simulated gust velocities from the filtered noise generators were processed to obtain power spectra. A typical sample is shown in Fig. 6 and shows excellent agreement between the samples taken and the theoretical spectrum of the filters in the frequency range 0.05–2.0 Hz (i.e., $0.7 \leq k' \leq 30$, for $u_0 = 430$, $L = 1000$). This is the frequency range where the filter closely simulates the Dryden spectrum, as is also indicated in Fig. 6.

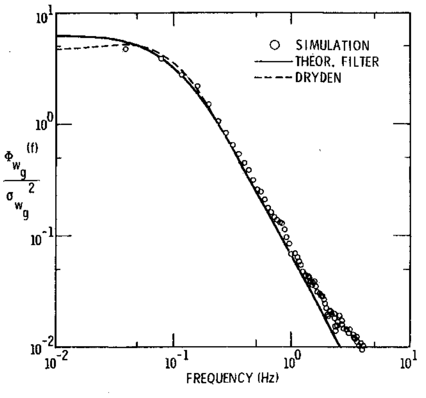

Fig. 6 Theoretical and simulated turbulence spectra.

Table 1 Physical dimensions of example airplane

Dimension	Wing	Stabilizer	Vertical tail
b, ft	160.0	50.35	22.7
$\bar{c}$, ft	22.2	10.3	18.5
S, sq ft	3228	483	416
$\lambda_{0.25\bar{c}}$, deg		25	35
$\lambda_{e.a.}$, deg		22.5	32.7
l (c.g. to 0.25 MAC), ft	0.0	74.7	64.6
h (c.g. to MAC), ft		27.39	15.11
l', (c.g. to e.a.)		71.9	60.7

Wind-Tunnel Results

The location of the three empennage bending moments are shown in Fig. 2 and their load coefficients are listed in Table 3 in nondimensionalized form (i.e., $C = BM/qS_W\bar{c}$). For the stabilizer bending moment, location 1, it is noted that the sideslip angle produces a load about 20% of that produced by angle of attack. Very little of this response to sideslip is attributable to the swept stabilizer by itself; most of the response appears to be a result of aerodynamic interference caused by the intersection of stabilizer and fin. The bending moment on the upper fin, location 2, is very close to the top and is therefore a measure of the unsymmetrical loads on the stabilizer (i.e., tailplane rolling moment) as a result of aerodynamic interference. This effect is seen to be about 40% of the fin root bending moment, location 3.

Tail Loads

The bending-moment responses to simultaneous vertical and lateral turbulence components were examined for significance of the nonlinear relationships considered. For this purpose, responses were obtained from the nonlinear simulation for three different levels of gust intensity. These responses were observed to be proportional to the gust intensity; mean-square values remained essentially zero; and probability distributions were constant and Gaussian. It is indicated, therefore, that the nonlinear effects are not significant and that, consequently, single values of $\bar{A}$ and N_0 are sufficient to define the load at a particular location.

The proper functioning of the simulation and of the associated program for statistical analysis was checked by comparing results from the linear version of the simulation with those from analytical solutions of the linearized equations. These results in the form of the ratio of the average frequency of crossing various bending-moment levels to that of crossing the zero level N/N_0, together with the results from the nonlinear simulation are shown in Fig. 7 for the stabilizer bending moment $BM1$. The simulation configurations are identified as 1) linear, 2) linear airframe motion equations and nonlinear tail-loads equations, and 3) nonlinear motion and loads equations. The close agreement of the data confirm both the performance of the simulation and the linear analysis as satisfactory for this particular airplane and flight condition.

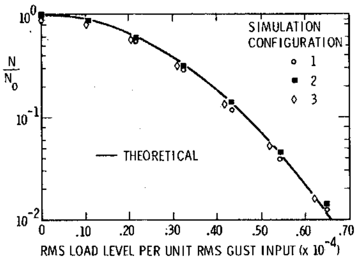

Fig. 7 Typical load level exceedance results (*BM*1).

Table 2a Flight parameters for example airplane

A, ft	10,000
u_0, fps	430
W, lb	180,000
L, ft	1,000
C_{L_0}	0.31
c.g., % MAC	25
i_H, rad	0
ϵ_0, rad	0.0349
$\partial\epsilon/\partial\alpha$	0.288

Table 2b Natural frequencies and damping ratios

	Short-period mode	Dutch roll mode
f_0, Hz	0.37	0.21
ζ	0.62	0.38

The results from linear analysis were then used to compare the load from simultaneous vertical and lateral turbulence components with the load from each component acting separately and to assess other loadings peculiar to the T-tail configuration. Pertinent results in terms of $\bar{A}$ and N_0 for fin and stabilizer bending moments from simultaneous turbulence components are given in Table 4. Values of $\bar{A}$ for the stabilizer bending moment for the vertical, lateral, and simultaneous gust velocity components are shown in Table 5.

With regard to loads on the fin, there is no evidence either on the basis of aerodynamic loads from the wind-tunnel tests or from the response calculations that there is any increase in load from simultaneous turbulence components over that from the lateral turbulence component only. There is, however, an additional load over that for a conventional tail due to the presence of the stabilizer above the fin. Part of this load is a bending moment imparted to the fin by a stabilizer rolling moment due to asymmetrical loading of the stabilizer from sideslip as was previously mentioned with respect to wind-tunnel test results in Table 3. The remainder of the additional fin load arises from inertia forces from the stabilizer. The extent of the total additional loading can be deduced from the values of $\bar{A}$ in Table 4 for $BM2$ and $BM3$. The bending moment $BM2$ is located at the top of the fin and, therefore, this moment is a result of the stabilizer aerodynamic and inertia rolling moment. For a conventional tail, any stabilizer rolling moment would be resisted by the fuselage, not the fin. Therefore, the ratio of root bending moment $BM3$ of the T-tail fin to that of a conventional fin is $\bar{A}_{BM3}/(\bar{A}_{BM3} - \bar{A}_{BM2})$. The magnitude of this ratio, based on values of $\bar{A}$'s from Table 4, is almost 2. The relative contributions of the asymmetrical aerodynamic forces and the inertia forces cannot be deduced from the $\bar{A}$ values because complex frequency relations exist between the two. However, the effect of stabilizer aerodynamic forces on the fin should be given consideration.

The magnitude of the stabilizer load from simultaneous vertical and lateral turbulence components relative to that from the vertical component only is indicated in terms of $\bar{A}$ for stabilizer bending moment $BM1$ in Table 5. Values are given for the Dryden spectrum and also for the more realistic von Kármán spectrum. The stabilizer bending moment for the simultaneous (total) turbulence components is greater than that for the vertical component alone by about 50% for the Dryden spectrum and by about 30% for the von Kármán spectrum. The relatively smaller contribution of the lateral component for the von Kármán spectrum reflects the lesser attenuation at the higher frequencies of this spectrum relative to the Dryden spectrum. In both cases, however, the lateral component contributes essentially as much to the stabilizer load as does the vertical component.

Table 3 Nondimensional empennage load coefficients from wind-tunnel tests

	Load coefficients, C_{ij}				
	Linear terms/rad		Nonlinear terms/rad^2		
BM Sta 1	A	B	A^2	AB	B^2
1	0.04118	0.008968	−0.01541	−0.02222	0.01803
2	...	−0.08072	...	0.07316	−0.1464
3	...	−0.2053	...	0.4713	...

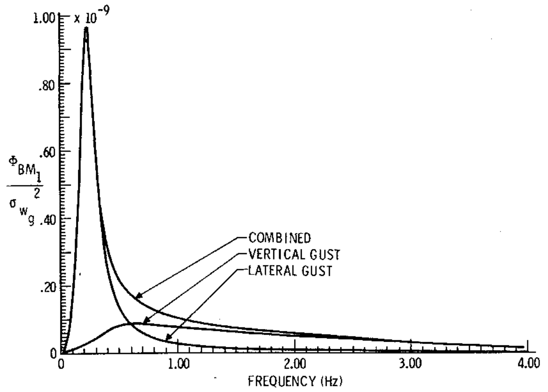

Fig. 8 **Vertical and lateral gust contributions to *BM*1 response spectrum.**

Some insight with regard to the physical reasons for the appreciable stabilizer bending moment from the lateral turbulence component relative to that from the vertical component can be obtained from the power spectra shown in Fig. 8. The spectrum for the total or combined load consists of the sum of the individual spectra from the uncorrelated vertical and lateral gust velocities. It is observed that the areas under the spectra (mean-square values) from the vertical and lateral gusts acting individually are approximately equal. However, most of the area associated with the lateral gust is concentrated in the frequency range below 0.6 Hz, whereas the area associated with the vertical gust is spread over a range of frequencies above about 0.5 Hz.

The shapes of the bending-moment spectra are determined for a given turbulence spectrum by the square of the modulus of the bending-moment frequency response functions. Examination of these functions in Fig. 9 reveals that the response to the lateral gust is maximum at the natural frequency of the Dutch roll mode, 0.26 Hz, whereas the response to the vertical gust exhibits no peak at the natural frequency of the short-period mode, 0.34 Hz. In fact, even though the damping ratio is less than critical (0.62), the response is very small in comparison to that at the larger frequencies. The lack of response to the vertical gust near the short-period mode frequency is due primarily to the phase shift accompanying

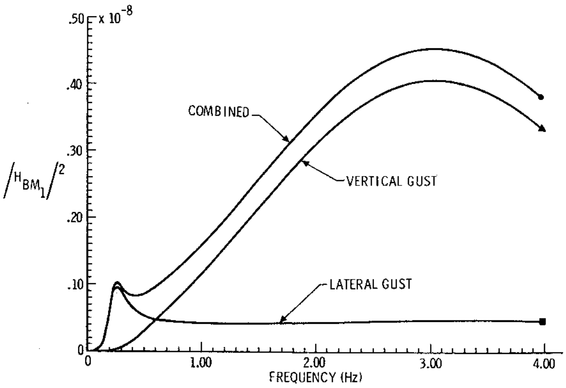

Fig. 9 **Frequency response functions (amplitude squared) for stabilizer bending moment *BM*1 from vertical and lateral gust velocities.**

Table 4 Results from linear analysis

BM Sta	$\bar{A} \times 10^5$/fps	N_0/sec
1	2.17	1.77
2	1.25	0.622
3	2.64	0.583

the lag of the gust field between the wing and the tail. The phase shift is such as to cause the tail loads due directly to the gust to oppose those from the tail motion for this particular configuration. The effects of this phasing are expected to vary with differing flight conditions and airplane configurations.

It should be noted that although the magnitude of the stabilizer bending-moment frequency response to the vertical gust is much higher than that to the lateral gust for frequencies greater than 1.5 Hz, the characteristic shape of the turbulence power spectrum heavily attenuates the response spectra at increasingly higher frequencies and results in response spectra from the vertical and lateral gusts having nearly the same area as illustrated in Fig. 8.

Generalization of the results obtained by analyzing a simplified model of a T-tail airplane must be considered with caution. Other geometric configurations, flight conditions, flexibility, and so forth, may have appreciably different gust response characteristics. However, the fact that a substantial increase in stabilizer loading by simultaneous gusts over the loading by the vertical gust only is indicated for one example, means that it would be wise to estimate the effects of simultaneous gust loading for the tails of other airplanes for which the gust loads might be critical.

Concluding Remarks

Table 5 Vertical and lateral gust component contributions to stabilizer bending moment, *BM*1

Gust model	Bending-moment contributions $\bar{A} \times 10^5$/fps Vertical	Lateral	Total
Dryden	1.474	1.598	2.174
von Kármán	1.922	1.630	2.520

A study of the loads due to gusts on the empennage of a rigid but otherwise representative T-tail transport indicated that the bending-moment responses to simultaneously acting vertical and lateral gust velocity components can be calculated by conventional linear system methods. Effects of nonlinearities in the airframe dynamics and the tail load equations were found to be insignificant.

Bending moments in the fin are not affected by the vertical gust component; however, an aerodynamic rolling moment on the stabilizer due to interference effects from the lateral gust component induces an additional bending moment in the fin.

The stabilizer loads created by simultaneous vertical and lateral gusts were found for the example airplane to be significantly higher than those from the vertical gust only. Although the present results may not apply to all T-tail airplanes and to all flight conditions, they do suggest that the effects of simultaneous gust velocities should not be ignored.

References

[1] National Transportation Safety Board, "Aircraft Accident Report," SA 393, FILE 1-0008, 1968, Dept. of Transportation.

[2] "Airworthiness Standards: Transport Category Airplanes," Federal Aviation Regulations, Pt. 25, 1964.

[3] Etkin, B., *Dynamics of Flight*, Wiley, New York, 1959.

[4] Houbolt, J. C., Steiner, R., and Pratt, K. G., "Dynamic Response of Airplanes to Atmospheric Turbulence Including Flight Data on Input and Response," TR R-199, 1964, NASA.

[5] Rice, S. O., "Mathematical Analysis of Random Noise," *Bell System Technical Journal,* Pts. I and II, Vol. 23, No. 3, July 1944, pp. 282–332; Pts. III and IV, Vol. 24, No. 1, Jan. 1945, pp. 46–156.